

# A general framework for compressed sensing and parallel MRI using annihilating filter based low-rank Hankel matrix

Kyong Hwan Jin, Dongwook Lee, and Jong Chul Ye

## Abstract

Parallel MRI (pMRI) and compressed sensing MRI (CS-MRI) have been considered as two distinct reconstruction problems. Motivated by recent breakthroughs such as SAKE (simultaneous autocalibrating and k-space estimation) or LORAKS (Low-rank modelling of local k-space neighborhoods), an annihilating filter based low-rank Hankel matrix approach (ALOHA) is proposed as a general framework which unifies pMRI and CS-MRI as a weighted k-space interpolation problem. Our framework exploits an annihilating filter relationship originating from the sparsity in the transform domain as well as from parallel acquisition physics. This results in a rank-deficient Hankel structured matrix, whose missing data can be recovered with a low rank structured matrix completion algorithm after a k-space weighting. In particular, when the underlying image can be sparsified with a wavelet transform, the low rank matrix completion problem can be solved with a multi-scale pyramid resulting in efficient computation. Using the theoretical results from the latest compressed sensing literatures, we showed that the required sampling rates for ALOHA in both single and parallel imaging are nearly optimal. Experimental results with in vivo data for single/multi-coil imaging as well as dynamic imaging confirmed that the proposed method outperforms the state-of-the-art pMRI and CS-MRI. By reformulating the pMRI and CS-MRI as a weighted k-space interpolation problem that can be solved using a low rank Hankel structured matrix completion, the generalized ALOHA framework provides better insight into MRI reconstruction problems.

## Index Terms

Parallel MRI, Compressed Sensing, Annihilating filter, Structured low rank block Hankel matrix completion, wavelets, Pyramidal representation

Correspondence to:

Jong Chul Ye, Ph.D.

Professor

Dept. of Bio and Brain Engineering, KAIST

291 Daehak-ro Yuseong-gu, Daejeon 305-701, Republic of Korea

Email: jong.ye@kaist.ac.kr

Tel: 82-42-350-4320

Fax: 82-42-350-4310

## I. INTRODUCTION

MRI is an imaging system that sequentially acquires k-space data corresponding to the Fourier transform of an object. This enables us to apply various advanced signal processing techniques. Recently, compressed sensing theory [1], [2] has been used in accelerated MRI [3]–[5]. Compressed sensing algorithms can restore original signals from much less k-space data by exploiting the sparsity of an unknown image in total variation (TV) or wavelet transform domains, and incoherent sampling schemes such as Gaussian random or Poisson disc are usually required. Accurate MRI reconstruction from less data makes compressed sensing a hot topic in the research community; thus, it has been applied across many different application areas such as in pediatric imaging [6], dynamic cardiac MRI [7]–[9], perfusion imaging [10], angiography [11], and so on.

On the other hand, parallel MRI (pMRI) [12]–[14] exploits the diversity in the coil sensitivity maps that are multiplied by an unknown image. This provides additional spatial information for the unknown image, resulting in accelerated MR data acquisition through k-space sample reduction. Representative parallel imaging algorithms such as SENSE (sensitivity encoding) [12] or GRAPPA (generalized autocalibrating partially parallel acquisitions) [13] require regularly sampled k-space data for computationally efficient reconstruction. Moreover, additional k-space data, the so-called auto calibration lines (ACS), are often required to estimate the coil sensitive maps or GRAPPA kernels [13].

Because the aim of the two approaches is accelerated acquisition by reducing the k-space data, extensive research efforts have been made to synergistically combine the two for further acceleration. One of the most simplest approaches can be a SENSE type approach that explicitly utilizes the estimated coil maps to obtain an augmented compressed sensing problem:

$$\min_{\mathbf{f}} \|W\mathbf{f}\|_1 \quad \text{subject to} \quad \mathbf{g} = \begin{bmatrix} \mathbf{g}_1 \\ \vdots \\ \mathbf{g}_r \end{bmatrix} = \begin{bmatrix} A[S_1] \\ \vdots \\ A[S_r] \end{bmatrix} \mathbf{f} \quad (1)$$

where  $\mathbf{f}$  and  $\mathbf{g}_i$  denote the unknown image and the k-space measurements from the  $i$ -th coil, respectively;  $A$  is a subsampled Fourier matrix;  $W$  is a sparsifying transform, and  $[S_i]$  denotes a diagonal matrix whose diagonal elements come from the  $i$ -th coil sensitivity map. The multichannel version of k-t FOCUSS [7] is one of the typical examples of such approaches. On the other hand,  $l_1$ -SPIRiT ( $l_1$ - iTerative Self-consistent Parallel Imaging Reconstruction) [15] utilizes the GRAPPA type constraint as an additional

constraint for a compressed sensing problem:

$$\min_F \|\Psi F\|_{1,2} \quad (2)$$

$$\text{subject to} \quad G = AF \quad (3)$$

$$\text{VEC}(F) = M \cdot \text{VEC}(F) \quad (4)$$

where  $F = [\mathbf{f}_1 \ \mathbf{f}_2 \ \cdots \ \mathbf{f}_r]$ ,  $G = [\mathbf{g}_1 \ \mathbf{g}_2 \ \cdots \ \mathbf{g}_r]$  and  $\Psi$  denote a discrete wavelet transform matrix, and  $M$  is an image domain GRAPPA operator, and  $\text{VEC}(\cdot)$  is the vectorization operator. In both approaches, an accurate estimation of coil sensitivity maps or GRAPPA kernel is important to fully exploit the coil sensitivity diversity.

In order to overcome these difficulties, calibration-less parallel imaging methods have been extensively investigated, among which SAKE (simultaneous autocalibrating and k-space estimation) [16] represents one of the first steps. In SAKE, the missing k-space elements are reconstructed by imposing the data consistency and the structural maintenance constraints of the block Hankel structure matrix. However, the origin of the low rankness in the Hankel structured matrix for the case of a single coil measurement was not extensively investigated, and it was not clear whether SAKE could outperform the compressed sensing approach when it is applied to single coil data. Haldar [17], [18] ingeniously discovered that a Hankel structured matrix constructed by a single coil k-space measurement is low-ranked when an unknown image has finite support or a slow-varying phase. Based on this observation, he developed the so called LORAKS (Low-rank modeling of local k-space neighborhoods) algorithm [17] and its parallel imaging version, P-LORAKS (Low-rank modelling of local k-space neighborhoods with parallel imaging data) [18]. However, it is not clear how the existing theory can deal with large classes of image models that are not sparse by themselves but can be sparsified using various transforms such as wavelet transforms or total variations (TV), etc.

Therefore, one of the main goals of this paper is to develop a more general theory that encompasses the existing approaches. Toward that goal, first, we confirm that SAKE and LORAKS are indeed special cases of a novel algorithm family, what we called ALOHA (Annihilating filter based LOW-rank Hankel matrix Approach). More specifically, we show that the sparsity in the image domain can be directly related to the existence of *annihilating filters* [19]–[21] in the k-space. Interestingly, the commutative relation between an annihilating filter and k-space measurements provides a rank-deficient Hankel structured matrix. This observation was first made by Haldar in the LORAKS algorithm [17], [18]. Our contribution here is a proof that the rank of the Hankel structured matrix is determined by the sparsity level in the image

domain and the number of required MR k-space measurements is proportional to  $ck \log^4 n_1$ , where  $k$  is the sparsity and  $n_1$  is the dimension of the k-space and  $c$  is some constant.

Another significant contribution of this paper is the generalization beyond the image domain sparsity. More specifically, if an image signal can be sparsified using transforms such as wavelets, TV, etc., we show that there exist annihilating filters and the corresponding low rank Hankel structured matrices in the *weighted* k-space domain. We verify that the rank of the resulting Hankel structured matrix is determined by the sparsity in the transform domain. Interestingly, when an image can be sparsified with wavelet transforms, we can prove that the low rank structured matrix completion problem can be equivalently represented with a pyramidal decomposition and scale dependent k-space weighting. Accordingly, a low rank matrix structured completion algorithm can be progressively applied for each level of the pyramid to reduce the overall computational burden while maintaining superior image quality.

Finally, we investigate multi-channel generalization to unify the parallel MRI with ALOHA. Specifically, we confirm that there exist additional inter-coil annihilating filter relationships that are unique in pMRI and derive a multi-coil extension of the generalized ALOHA scheme. If the uniform weighting scheme is used, then the construction of the stacked Hankel matrix turns out to be equivalent to those of SAKE and P-LORAKS. We further substantiate that the multi-channel stacking of the weighted Hankel structure matrix may fully exploit the coil diversity thanks to the relationship to the algebraic bound of multiple measurement vector (MMV) compressed sensing [22]–[24].

Because sparsity in the wavelet domain or TV is the main property that has been exploited by existing compressed sensing approaches, our generalized ALOHA framework can compete with the existing CS-MRI algorithms, as demonstrated by our *in vivo* experiments. Another important advantage of the proposed algorithm is that, compared to the existing CS-MRI, the reconstruction errors are usually scattered throughout the entire images rather than exhibiting systematic distortion along edges because the annihilating filter relationships are powerful in estimating the edge signals. Given that many diagnostic errors are caused by the systematic distortion of images, we believe that our generalized ALOHA framework may have great potential in clinical applications.

## II. THEORY

### A. Fundamental Duality between Sparsity and Low-Rankness

This section describes the fundamental dual relationship between sparsity and low rankness in reciprocal domain, which is the key idea of the proposed algorithm. For better readability, the theory here is outlined by assuming 1-D signals, but the principle can be extended for multidimensional signals.

Consider a signal  $f(x)$  that is composed of a set of  $k$ -Diracs within a support set  $[0, \tau]$ :

$$f(x) = \sum_{j=0}^{k-1} c_j \delta(x - x_j) \quad x_j \in [0, \tau]. \quad (5)$$

Without loss of generality, we set  $\tau = n_1$  for a positive integer  $n_1 \in \mathbb{Z}$ . Then, the resulting Fourier transform signal is given by

$$\hat{f}(\omega) = \sum_{j=0}^{k-1} c_j e^{-i\omega x_j}. \quad (6)$$

In standard Nyquist sampling, we should measure discrete set of Fourier samples at  $\{\omega_i\}_{i=1}^m$  from a deterministic grid, whose grid size should be set to the Nyquist limit  $\Delta = 2\pi/n_1$  to avoid aliasing artifacts; so the k-space measurement can be represented as

$$\hat{f}[m] := \hat{f}(\omega) \Big|_{\omega=m\Delta} = \sum_{j=0}^{k-1} c_j e^{-i2\pi m x_j / n_1}, \quad m \in [0, \dots, n_1 - 1]. \quad (7)$$

The discrete spectral sampling model in Eq. (7) implies that the unknown signal in the image domain is an infinite periodic streams of Diracs with a period  $n_1$ , which is indeed a signal with the finite rate of innovation (FRI) with rate  $\rho = 2k/n_1$  [19]–[21]. Therefore, theoretical results from the FRI sampling theory can be used [19]–[21]. In particular, the FRI sampling theory tells us that we can find a minimum length *annihilating filter*  $\hat{h}[n]$  such that

$$(\hat{h} * \hat{f})[n] = \sum_{l=0}^k \hat{h}[l] \hat{f}[n - l] = 0, \quad \forall n. \quad (8)$$

The specific form of the annihilating filter  $\hat{h}[n]$  for the case of (7) is given in Appendix for completeness. By sampling the time domain signal at the rate of innovations, the authors in [19]–[21] proved that the perfect recovery is guaranteed from noiseless measurement.

However, classical FRI sampling theory is quite limited for highly accelerated MRI, because FRI sampling theory was developed for time domain sampling. To extend the applicability of the theory beyond the time domain, here we propose a generalization to the k-space sampling. Specifically, if  $\hat{h}[n]$  is a minimum length annihilating filter with  $k + 1$  filter taps, then for any  $k_1 \geq 1$  tap filter  $\hat{a}[n]$ , it is easy to see that the following filter with  $\kappa = k + k_1$  taps is also an annihilating filter for  $\hat{f}[n]$ :

$$\hat{h}_a[n] = (\hat{a} * \hat{h})[n]. \quad (9)$$

Accordingly, by removing the boundary data from the convolution, we can construct the following matrix

equation:

$$\mathcal{H}(\hat{\mathbf{f}})\bar{\mathbf{h}}_a = \mathbf{0}, \quad (10)$$

where the Hankel structure matrix  $\mathcal{H}(\hat{\mathbf{f}})$  is constructed as

$$\mathcal{H}(\hat{\mathbf{f}}) = \begin{bmatrix} \hat{f}[0] & \hat{f}[1] & \cdots & \hat{f}[\kappa-1] \\ \hat{f}[1] & \hat{f}[2] & \cdots & \hat{f}[\kappa] \\ \vdots & \vdots & \ddots & \vdots \\ \hat{f}[n_1-\kappa] & \hat{f}[n_1-\kappa+1] & \cdots & \hat{f}[n_1-1] \end{bmatrix} \in \mathbb{C}^{(n_1-\kappa+1) \times \kappa}. \quad (11)$$

and  $\bar{\mathbf{h}}_a$  denotes a vector that reverses the order of the elements in  $\hat{\mathbf{h}}_a \in \mathbb{C}^\kappa$ :

$$\hat{\mathbf{h}}_a = [\hat{h}_a[0] \ \cdots \ \hat{h}_a[\kappa-1]]^T \quad (12)$$

Then, we have the following result:

**Proposition 2.1.** *Let  $k$  denotes the number of Diracs within the support  $[0, n_1]$ . Suppose, furthermore,  $\kappa$  is given by  $(n_1 + 1)/2 \geq \kappa \geq k + 1$ . Then, for a given  $(n_1 - \kappa + 1) \times \kappa$  size Hankel structured matrix  $\mathcal{H}(\hat{\mathbf{f}})$  in (11), we have*

$$\text{RANK} \mathcal{H}(\hat{\mathbf{f}}) = k, \quad (13)$$

where  $\text{RANK}(\cdot)$  denotes a matrix rank.

*Proof.* Note that (12) can be represented as

$$\hat{\mathbf{h}}_a = \mathcal{C}(\hat{\mathbf{h}})\hat{\mathbf{a}} \quad (14)$$

where  $\hat{\mathbf{a}} = [\hat{a}[0] \ \cdots \ \hat{a}[k_1-1]]$  and  $\mathcal{C}(\hat{\mathbf{h}}) \in \mathbb{C}^{\kappa \times k_1}$  is a Toeplitz structured convolution matrix from  $\hat{\mathbf{h}}$ :

$$\mathcal{C}(\hat{\mathbf{h}}) = \begin{bmatrix} \hat{h}[0] & 0 & \cdots & 0 \\ \hat{h}[1] & \hat{h}[0] & \cdots & 0 \\ \vdots & \vdots & \ddots & \vdots \\ \hat{h}[k-1] & \hat{h}[k-2] & \cdots & \hat{h}[k-k_1] \\ \vdots & \vdots & \ddots & \vdots \\ 0 & 0 & \cdots & \hat{h}[k-1] \end{bmatrix} \in \mathbb{C}^{\kappa \times k_1} \quad (15)$$

where  $\kappa = k + k_1$ . Since  $\mathcal{C}(\hat{\mathbf{h}})$  is a convolution matrix, it is full ranked and we can show that

$$\dim \mathcal{C}(\hat{\mathbf{h}}) = k_1,$$

where  $\dim(\cdot)$  denotes the dimension of a matrix. Moreover, the range space of  $\mathcal{C}(\hat{\mathbf{h}})$  now generates the

null space of the Hankel matrix, so it is easy to show

$$\dim \mathcal{C}(\hat{\mathbf{h}}) = \dim \text{NUL} \mathcal{H}(\hat{\mathbf{f}}) = k_1,$$

where  $\text{NUL}(\cdot)$  represent a null space of a matrix. Owing to the condition  $(n_1 + 1)/2 \geq \kappa$ , the number of columns in  $\mathcal{H}(\hat{\mathbf{f}})$  cannot be larger than that of rows. Hence, we have

$$\text{RANK} \mathcal{H}(\hat{\mathbf{f}}) = \kappa - k_1 = k, \quad (16)$$

which is equal to the sparsity level. This concludes the proof.  $\square$

Proposition 2.1 implies the following fundamental duality:

$$k\text{-sparse signal} \xleftrightarrow{\mathcal{F}} k\text{-ranked Hankel structured matrix},$$

where  $\mathcal{F}$  denotes the Fourier transform. Therefore, if some of the Hankel matrix elements are missing and one can measure samples only on the index set  $\Omega$ , the fundamental duality suggests a way to recover these elements, which is based on low rank matrix completion [25]–[29]. Among various type of matrix completion algorithm, one of the most well-characterised approaches is a convex relaxation approach using the nuclear norm [25], [26], [28], [29]. More specifically, the missing k-space elements can be found by solving the following nuclear norm minimization problem:

$$\begin{aligned} (P) \quad & \min_{\mathbf{m} \in \mathbb{C}^{n_1}} \quad \|\mathcal{H}(\mathbf{m})\|_* \\ & \text{subject to} \quad P_{\Omega}(\mathbf{m}) = P_{\Omega}(\hat{\mathbf{f}}) \end{aligned} \quad (17)$$

where  $\|\cdot\|_*$  denotes the matrix nuclear norm and  $P_{\Omega}$  is the projection operator on the k-space sampling index set  $\Omega$ . One of the most important contributions of this paper is to show that the formulation (P) for MRI provides nearly same optimal sampling rate as in the standard compressed sensing MR approach:

**Theorem 2.2.** *Suppose that the sampling index set  $\Omega$  is chosen randomly among  $[0, n_1 - 1]$  and  $|\Omega| = m$ . Then, if the number of spectral sample  $m$  is given by*

$$m > c_1 \mu_1 c_s k \log^4(n_1) \quad (18)$$

for some constant  $c_1$  and an incoherence parameter  $\mu_1$ , and

$$c_s = \max\{n_1/\kappa, n_1/(n_1 - \kappa + 1)\}, \quad (19)$$

then the perfect recovery of the missing spectral components is possible with a probability exceeding  $1 - n_1^{-2}$ .

*Proof.* Thanks to (7), the explicit representation of  $\mathcal{H}(\hat{\mathbf{f}})$  is given by

$$\mathcal{H}(\hat{\mathbf{x}}) = L D R^T \quad (20)$$

where

$$L = \begin{bmatrix} 1 & 1 & \cdots & 1 \\ y_0 & y_1 & \cdots & y_{k-1} \\ \vdots & \vdots & \ddots & \vdots \\ y_0^{n_1-\kappa} & y_1^{n_1-\kappa} & \cdots & y_{k-1}^{n_1-\kappa} \end{bmatrix} \in \mathbb{C}^{(n_1-\kappa+1) \times k} \quad (21)$$

$$R = \begin{bmatrix} 1 & 1 & \cdots & 1 \\ y_0 & y_1 & \cdots & y_{k-1} \\ \vdots & \vdots & \ddots & \vdots \\ y_0^{\kappa-1} & y_1^{\kappa-1} & \cdots & y_{k-1}^{\kappa-1} \end{bmatrix} \in \mathbb{C}^{\kappa \times k} \quad (22)$$

and

$$D = \begin{bmatrix} c_0 & 0 & \cdots & 0 \\ 0 & c_1 & \cdots & 0 \\ \vdots & \vdots & \ddots & \vdots \\ 0 & 0 & \cdots & c_{k-1} \end{bmatrix}, \quad (23)$$

and  $y_j = e^{-i2\pi x_j/n_1}$  for  $j = 0, \dots, k-1$ . Note that (20) is equivalent to the 1-D version of (in fact, a transposed) enhanced matrix in the spectral compressed sensing with the enhanced matrix completion (EMaC) (Eq. (11) in [30]). Therefore, we can employ the theoretical results in [30]. Specifically, using the powerful dual certificate and golfing scheme originally developed by David Gross [28], Chen and Chi [30] showed that if the number of spectral sample  $m$  is given by

$$m > c_1 \mu_1 c_s k \log^4(n_1) \quad (24)$$

for some constant  $c_1$ , and

$$c_s = \max\{n_1/\kappa, n_1/(n_1 - \kappa + 1)\} \quad (25)$$

and the incoherence parameter  $\mu_1$  given by

$$\sigma_{\min}(L^*L) \geq \frac{n_1 - \kappa + 1}{\mu_1}, \quad \sigma_{\min}(R^*R) \geq \frac{\kappa}{\mu_1}, \quad (26)$$

then the perfect recovery of the missing spectral components is possible with a probability exceeding  $1 - n_1^{-2}$ . This concludes the proof.  $\square$

The annihilating filter size  $\kappa$  corresponds to the ‘‘matrix pencil parameter’’ [31] in the spectral compressed sensing approach by Chen and Chi [30], who also showed that the incoherence parameter  $\mu_1$  in (18) grows to one as the annihilating filter size  $\kappa$  increases [30]. Hence, the sampling rate in (18) is

nearly optimal since it is proportional to the unknown sparsity level except  $\log^4(\cdot)$  factor. This suggest the following important observation: by reformulating the compressed sensing problem as a low rank Hankel structured matrix completion problem in the measurement domain, no performance loss can be expected. In fact, this *low rank Fourier interpolation* approaches has many advantages over the standard compressed sensing as will be discussed later.

Note that LORAKS [17], [18] and the single coil version of SAKE [16] are basically similar to (P) even though their construction of the Hankel structure matrix is slightly different and they employed non-convex version of low rank matrix completion (see Methods section). Therefore, we call this class of algorithms as ALOHA family.

### B. Generalized ALOHA

In general, signals may not be sparse in the image domain, but can be sparsified in a transform domain. Our goal is to find a generalized ALOHA framework whose sampling rate can be reduced down to the transform domain sparsity level. Toward this goal, we adopt one of the most general sparse signal models from the theory of *sparse stochastic processes* [32], [33]. Specifically, the signal  $f$  of our interest is assumed to satisfy the following stochastic partial differential equation:

$$Lf = w \quad (27)$$

where  $L$  denotes a constant coefficient linear differential equation (or whitening operator in [32], [33]):

$$L := a_K \partial^K + a_{K-1} \partial^{K-1} + \dots + a_1 \partial + a_0 \quad (28)$$

and  $w$  is a driving continuous domain signal (or white noises in [32], [33]). In this paper, we are particularly interested in the following form of the sparse driving signal

$$w(x) = \sum_{j=0}^{k-1} c_j \delta(x - x_j) \quad x_j \in [0, n_1]. \quad (29)$$

This model includes many class of signals with finite rate of innovations [19]–[21]. For example, if the underlying signal is piecewise constant, we can set  $L$  as the first differentiation. In this case,  $f$  corresponds to the total variation signal model. In the following, we provide two alternative reconstruction options of the sparse signal  $f$  that is described by (27).

1) *Operator weighting*: By taking the Fourier transform of (27), we have

$$\mathcal{F}\{Lf(x)\} = \hat{l}(\omega) \hat{f}(\omega) = \sum_{j=0}^{k-1} a_j e^{-i\omega x_j} \quad (30)$$

where

$$\hat{l}(\omega) = a_K(i\omega)^K + a_{K-1}(i\omega)^{K-1} + \dots + a_1(i\omega) + a_0 \quad (31)$$

Accordingly, the same filter  $\hat{h}[n]$  that annihilates (7) can annihilate the weighted signal  $\hat{l}(\omega)\hat{f}(\omega)$ . Therefore, we can estimate the unknown k-space samples by solving the following generalized ALOHA problem and undoing the weighting by  $\hat{\mathbf{l}}$ :

$$\begin{aligned} (P_{gALOHA}) \quad & \min_{\mathbf{m} \in \mathbb{C}^{n_1}} \quad \|\mathcal{H}(\mathbf{m})\|_* \\ & \text{subject to} \quad P_\Omega(\mathbf{m}) = P_\Omega(\hat{\mathbf{l}} \odot \hat{\mathbf{f}}) , \end{aligned} \quad (32)$$

where  $\odot$  denotes the Hadamard product, and  $\hat{\mathbf{l}}$  and  $\hat{\mathbf{f}}$  denotes the vectors composed of discrete samples of  $\hat{l}(\omega)$  and  $\hat{f}(\omega)$ , respectively, which can be represented as follows:

$$\hat{\mathbf{l}} = [\hat{l}[0] \quad \dots \quad \hat{l}[n_1]]^T \quad (33)$$

$$\hat{\mathbf{f}} = [\hat{f}[0] \quad \dots \quad \hat{f}[n_1]]^T . \quad (34)$$

2) *Wavelet analysis*: In fact, the signal  $f$  in (27) can be sparsified using wavelet transform as demonstrated in [32], [33]. Since the sparsity in wavelet domain have been the main interest in the existing compressed sensing theory, we are particularly interested in this analysis approach. Interestingly, the resulting generalized ALOHA framework has very unique pyramidal structure that allows computational efficient and noise robust implementation of a low rank Hankel matrix completion algorithm.

Specifically, we assume that we have some real-valued ‘‘L-compatible’’ generalized wavelet [32], [33] which, at a given resolution level  $s$ , are such that

$$\psi_s(x) = L^* \phi_s(x) . \quad (35)$$

Here,  $L^*$  is the adjoint operator of  $L$  and  $\phi_s$  is some smoothing kernel with a good localisation property. In dyadic wavelet decomposition, typically, we have  $\phi_s(x) = 2^{-s/2} \phi_o(x/2^s)$ .

We further assume that the wavelet is a cardinal wavelet, i.e. its smoothing kernel has knots position

on integer indices. Using (35), the wavelet analysis of the signal  $f(x)$  in (27) is given by

$$\begin{aligned}
\langle f, \psi_s(\cdot - x) \rangle &= \langle f, L^* \phi_s(\cdot - x) \rangle \\
&= \langle Lf, \phi_s(\cdot - x) \rangle \\
&= \langle w, \phi_s(\cdot - x) \rangle = (\bar{\phi}_s * w)(x) \\
&= \sum_{j=0}^{k-1} c_j \bar{\phi}_s(x - x_j)
\end{aligned} \tag{36}$$

where  $\bar{\phi}_s(x) = \phi_s(-x)$  is the reversed version of  $\phi_s$ .

Due to the dyadic wavelet decomposition, the discrete samples are given by

$$f^s[l] := \langle f, \psi_s(\cdot - x) \rangle|_{x=2^s l}, \quad l \in [0, \dots, n_1/2^s - 1], \tag{37}$$

and the corresponding discrete time Fourier transform (DTFT) is given by

$$\begin{aligned}
\hat{f}^s(e^{i\omega}) &:= \sum_l f^s[l] e^{-i\omega 2^s l} \\
&= \frac{1}{2^s} \sum_{n=0}^{2^s-1} \hat{\psi}_s^* \left( \omega + n \frac{2\pi}{2^s} \right) \hat{f} \left( \omega + n \frac{2\pi}{2^s} \right) \\
&= \frac{1}{\sqrt{2^s}} \sum_{n=0}^{2^s-1} \hat{\psi}^*(2^s \omega + 2\pi n) \hat{f} \left( \omega + n \frac{2\pi}{2^s} \right), \quad \text{where } |\omega| \leq \pi/2^s.
\end{aligned} \tag{38}$$

where we use  $\hat{\psi}_s^*(\omega + n \frac{2\pi}{2^s}) = \sqrt{2^s} \hat{\psi}^*(2^s \omega + 2\pi n)$  and the righthand side terms of (39) come from spectral copies due to the downsampling. Hence, if we choose maximally localised smoothing function  $\bar{\phi}_s$ , then the discrete sample (37) can be made as sparse as possible. Specifically, the following triangle basis function was suggested as a smoothing kernel with a good localization property [32], [33]:

$$\phi_0(x) = \beta_+^1(2x) \tag{40}$$

where

$$\beta_+^1(x) = \begin{cases} x, & 0 \leq x < 1 \\ 2 - x, & 1 \leq x < 2 \\ 0, & \text{otherwise} \end{cases}$$

Furthermore, when  $L = \frac{\partial}{\partial x}$ , then this choice of the smoothing kernel produces the Haar wavelet [32]:

$$\psi_0(x) = L^* \beta_+^1(2x) = \begin{cases} 1, & 0 \leq x < \frac{1}{2} \\ -1, & \frac{1}{2} \leq x < 1 \\ 0, & \text{otherwise} \end{cases}, \tag{41}$$

which is used throughout the paper.

If the number of nonzero coefficient  $f^s[l]$  is small, then the form of the left hand side of (38) is similar to (7), so annihilating filters and the corresponding low-rank Hankel matrix can be found. One technical

issue is that the righthand side of (39) has aliased copies of k-space data weighted by wavelet weighting. Therefore, the direct application of low rank matrix completion may not work.

One remarkable observation of (38) is that the  $2\pi/2^s$  repeating spectral structure implies a *pyramidal* decomposition of the Hankel structured matrix. More specifically, if the spectral component of  $\hat{f}(\omega)$  is estimated for  $|\omega| \geq \pi/2^s$  from (38), then we can constitute a residual signal recursively:

$$\hat{f}_r(\omega) := \begin{cases} 0, & |\omega| \geq \pi/2^s \\ \hat{f}(\omega), & \text{otherwise} \end{cases} \quad (42)$$

Then, for the corresponding discrete sample  $f_r^s[l] := \langle f_r, \psi_s(\cdot - x) \rangle|_{x=2^s l}$  with  $f_r = \mathcal{F}^{-1}\{\hat{f}_r\}$ , we have

$$\hat{f}_r^s(\omega) := \sum_l f_r^s[l] e^{-i\omega 2^s l} = \frac{1}{\sqrt{2^s}} \hat{\psi}^*(2^s \omega) \hat{f}(\omega), \quad (43)$$

because its high frequency content will no more alias at a frequency inside  $|\omega| \leq \pi/2^s$ .

Now, due to the sparsity of  $f_r^s[l]$ , there exists a filter that annihilates  $\hat{\psi}^*(2^s \omega) \hat{f}(\omega)$ . Consequently, the  $s$ -scale generalized ALOHA problem can be formulated as

$$\begin{aligned} \min_{\mathbf{m} \in \mathbb{C}^{n_1/2^s}} \quad & \|\mathcal{H}(\mathbf{m})\|_* \\ \text{subject to} \quad & P_\Omega(\mathbf{m}) = P_\Omega(\hat{\mathbf{I}}^s \odot \hat{\mathbf{f}}^s) . \end{aligned} \quad (44)$$

where

$$\hat{f}^s[n] = \hat{f}(\omega) \Big|_{\omega=n\pi/n_1}, \quad n = -\frac{n_1}{2^{s+1}}, \dots, \frac{n_1}{2^{s+1}} - 1 . \quad (45)$$

and the weighting vector  $\hat{\mathbf{I}}^s$  is composed of following spectral samples :

$$\begin{aligned} \hat{l}^s[n] &= \hat{l}^s(\omega) \Big|_{\omega=n\pi/n_1} \\ &= \frac{1}{\sqrt{2^s}} \hat{\psi}^*(2^s \omega) \Big|_{\omega=n\pi/n_1}, \quad n = -\frac{n_1}{2^{s+1}}, \dots, \frac{n_1}{2^{s+1}} - 1 , \end{aligned} \quad (46)$$

where the superscript  $*$  denotes the complex conjugate. Note that sampling interval for  $\hat{\psi}^*(\omega)$  widens by factor of 2 for each successive scale to construct the k-space weighting vector  $\hat{\mathbf{I}}^s$ , although it is not the case for the data vector  $\hat{\mathbf{f}}^s$ .

Consequently, we have a pyramidal decomposition as shown in Fig. 1, and the generalized ALOHA (44) should be solved from the lowest scale, i.e.  $s = 0$ , up to the highest scale (see Methods for more discussion of the figures). Moreover, because sparsity can be imposed only on the wavelet coefficients, the low frequency k-space data that correspond to the scaling function coefficients should be acquired additionally during MR data acquisition. This information as well as the annihilating filter size then determines the the depth of the pyramidal decomposition. We will discuss this in detail later.

There are several advantages of using wavelet approaches compared to the direct operator weighting in ALOHA framework. First, the pyramidal decomposition structure for low rank matrix completion can significantly reduce the overall computational complexity. Moreover, it has been observed in [32], [33] that the wavelet approach is more robust for noise and the model mismatch, which is also consistently observed in ALOHA framework as will be discussed later.

We are aware that a two-level decomposition was used for low-rank MRI [34]. However, in [34], the relationship to wavelet transform and the optimal decomposition level were not clearly identified.

### C. Multi-channel Generalization

Beside the annihilation property originating from sparsity in the transform domain, there exists an additional annihilation relationship that is unique in parallel MRI. The relationship we described here is indeed what has been explored in SAKE and P-LORAKS using a uniform k-space weighting (even though they were inspired by the null space or GRAPPA type relationship), and our contribution is a theoretical interpretation for general k-space weighting schemes.

Specifically, in pMRI, the unknown image  $g_i(x)$  from the  $i$ -th coil can be represented as

$$g_i(x) = s_i(x)f(x), \quad i = 1, \dots, r,$$

where  $s_i(x)$  denotes the  $i$ -th coil sensitivity map,  $f(x)$  is an unknown image, and  $r$  denotes the number of coils. Then, for the given operator  $L$  in (28), we have

$$Lg_i(x) = \sum_{j=0}^K a_j \partial^j (s_i(x)f(x)) \quad (47)$$

$$= \sum_{j=0}^K a_j \sum_{p+q=j} \frac{j!}{p!q!} \partial^p s_i(x) \partial^q f(x) \quad (48)$$

$$= s_i(x)Lf(x) + \sum_{j=1}^K a_j \left( \sum_{p+q=j, p \geq 1} \frac{j!}{p!q!} \partial^p s_i(x) \partial^q f(x) \right), \quad (49)$$

where the second equality comes from Leibniz's rule for partially differentiating a product of functions. If we further assume that the coil sensitivity map  $s_i(x)$  varies more slowly such that  $\partial s_i(x) \simeq 0$ , then we have the following approximation:

$$Lg_i(x) \simeq s_i(x)Lf(x), \quad i = 1, \dots, r.$$

Assuming that the approximation is sufficiently accurate, it is easy to see the following inter-coil relation:

$$s_j(x)Lg_i(x) = s_i(x)Lg_j(x), \quad i, j = 1, \dots, r, \text{ and } i \neq j, \quad (50)$$

which can be equivalently represented in Fourier domain as

$$\hat{s}_j(\omega) * \left( \hat{l}(\omega) \hat{g}_i(\omega) \right) - \hat{s}_i(\omega) * \left( \hat{l}(\omega) \hat{g}_j(\omega) \right) = 0, \quad i \neq j, \quad \forall \omega. \quad (51)$$

Consequently, Hankel matrix from each channel can be stacked side by side to form a matrix  $\mathcal{Y}$ :

$$\mathcal{Y} = [\mathcal{H}(\hat{\mathbf{1}} \odot \hat{\mathbf{g}}_1) \quad \cdots \quad \mathcal{H}(\hat{\mathbf{1}} \odot \hat{\mathbf{g}}_r)] \in \mathbb{C}^{(n_1 - \kappa + 1) \times \kappa r}, \quad (52)$$

and the multichannel version of the generalized ALOHA becomes

$$\begin{aligned} \min_{\{\mathbf{m}_i\}_{i=1}^r} & \quad \left\| [\mathcal{H}(\mathbf{m}_1) \quad \cdots \quad \mathcal{H}(\mathbf{m}_r)] \right\|_* \\ \text{subject to} & \quad P_\Omega(\mathbf{m}_i) = P_\Omega(\hat{\mathbf{1}} \odot \hat{\mathbf{g}}_i), \quad i = 1, \dots, r. \end{aligned} \quad (53)$$

Here, the augmented matrix  $\mathcal{Y}$  in (52) has the following rank condition:

**Lemma 2.3.** *For the concatenated Hankel matrix given in (52), we have*

$$\text{rank } \mathcal{Y} \leq \frac{r(2k - r + 1)}{2}. \quad (54)$$

where  $k$  and  $r$  denotes the sparsity and the number of coils, respectively.

*Proof.* Since Eq. (51) holds for every pair among  $r$ -channels, it is easy to show that

$$\mathcal{Y} \mathcal{S}_1 = \mathbf{0},$$

where  $\mathcal{S}_1$  is defined recursively as follows:

$$\mathcal{S}_{r-1} \triangleq \begin{bmatrix} \hat{\mathbf{s}}_r \\ -\hat{\mathbf{s}}_{r-1} \end{bmatrix} \quad (55)$$

$$\mathcal{S}_t \triangleq \left[ \begin{array}{cccc|c} \hat{\mathbf{s}}_{t+1} & \hat{\mathbf{s}}_{t+2} & \cdots & \hat{\mathbf{s}}_C & \mathbf{0} \\ -\hat{\mathbf{s}}_t & & & & \mathcal{S}_{t+1} \\ & -\hat{\mathbf{s}}_t & & & \\ & & \ddots & & \\ & & & -\hat{\mathbf{s}}_t & \end{array} \right], \quad (56)$$

Accordingly,

$$\dim \text{NUL}(\mathcal{Y}) = \text{rank}(\mathcal{S}_1) = \binom{r}{2} = r(r-1)/2.$$

Furthermore, Proposition 2.1 informs us that  $\mathcal{H}(\hat{\mathbf{1}} \odot \hat{\mathbf{g}}_i)$  in  $\mathcal{Y}$  has rank  $k$ . Therefore, we have

$$\text{rank } \mathcal{Y} \leq kr - \frac{r(r-1)}{2} \quad (57)$$

$$= \frac{r(2k - r + 1)}{2}. \quad (58)$$

This concludes the proof.  $\square$

Because the rank of  $\mathcal{Y}$  is  $r(2k - r + 1)/2$  and there exist additional degrees of freedom that belong to the amplitudes of Diracs in the transform domain, the total degrees of the freedom for the FRI signal are  $r(2k - r + 1)$  [19]–[21]. In parallel MRI, if  $m$  denotes the number of k-space sampling locations, then k-space data are sampled simultaneously from  $r$ -coils and the total number of k-space samples becomes  $mr$ . Since the number of the samples should be larger than the degree of the freedom, we have

$$mr \geq r(2k - r + 1) \iff k \leq \frac{m + r - 1}{2}. \quad (59)$$

This result has very important geometric meaning. Suppose that we attempt to address parallel imaging by exploiting the joint sparsity. Using the notation in (1), this can be addressed by the following multiple measurement vector (MMV) problem

$$\begin{aligned} \min_F \quad & \|F\|_0 \\ \text{subject to} \quad & G = AF \end{aligned} \quad (60)$$

where  $G = [\mathbf{g}_1, \dots, \mathbf{g}_r]$  and  $F = [\mathbf{f}_1, \dots, \mathbf{f}_r]$  with  $\mathbf{f}_i = [S_i]\mathbf{f}$  for a given sensitivity map  $[S_i]$ . Then, it was shown in [22]–[24] that if  $F_*$  satisfies  $AF_* = G$  and

$$\|F_*\|_0 < \frac{\text{spark}(A) + \text{RANK}(G) - 1}{2} \quad (61)$$

then  $F_*$  is the unique solution for  $G = AF$ , where  $\text{spark}(A)$  denote the smallest number of linearly dependent columns of  $A$ . For randomly chosen Fourier samples, we have  $\text{spark}(A) \geq m + 1$ . Moreover,  $\text{RANK}(G) = r$ . Hence, (61) is equivalent to (59) if the unknown sparsity level is  $k$ , i.e.  $\|F_*\|_0 = k$ . Therefore, our ALOHA formulation for multichannel measurement using the formulation (53) may fully exploit the multi-channel diversity from parallel acquisition.

### III. METHODS

#### A. 2D Hankel Structured Matrix Construction

In multi-slice or dynamic acquisition of MR data, the readout direction is usually fully sampled and the other two encoding directions are under sampled. Therefore, this section presents an explicit way of constructing a 2D Hankel structured matrix. If  $\hat{h}[n, m]$  is a  $p_1 \times q_1$  size 2D annihilating filter, then the corresponding annihilating filter relation is given by

$$(\hat{h} * \hat{f})[n, m] = \sum_{i=0}^{p_1-1} \sum_{j=0}^{q_1-1} \hat{h}[i, j] \hat{f}[n - i, m - j] = 0, \quad \forall n, m \in \Omega. \quad (62)$$

Let  $n_1 \times m_1$  k-space data matrix be defined by

$$\hat{F} := \begin{bmatrix} \hat{f}[0,0] & \cdots & \hat{f}[0,m_1-1] \\ \vdots & \ddots & \vdots \\ \hat{f}[n_1-1,0] & \cdots & \hat{f}[n_1-1,m_1-1] \end{bmatrix} = [\hat{\mathbf{f}}_0 \cdots \hat{\mathbf{f}}_{m_1-1}] \quad (63)$$

Similarly, we define  $p_1 \times q_1$  annihilating filter matrix  $\hat{H}$ . Then, by removing the boundary effect from the 2D convolution as shown in Fig. 2(a), the 2D annihilation property should hold only inside of the domain and (62) can be equivalently represented as

$$\mathcal{H}(\hat{F})\hat{\mathbf{h}} = \mathbf{0}, \quad (64)$$

where a 2-D Hankel structured matrix  $\mathcal{H}(\hat{F})$  is constructed as

$$\mathcal{H}(\hat{F}) = \begin{bmatrix} \mathcal{H}(\hat{\mathbf{f}}_0) & \mathcal{H}(\hat{\mathbf{f}}_1) & \cdots & \mathcal{H}(\hat{\mathbf{f}}_{q_1-1}) \\ \mathcal{H}(\hat{\mathbf{f}}_1) & \mathcal{H}(\hat{\mathbf{f}}_2) & \cdots & \mathcal{H}(\hat{\mathbf{f}}_{q_1}) \\ \vdots & \vdots & \ddots & \vdots \\ \mathcal{H}(\hat{\mathbf{f}}_{m_1-q_1}) & \mathcal{H}(\hat{\mathbf{f}}_{m_1-q_1+1}) & \cdots & \mathcal{H}(\hat{\mathbf{f}}_{m_1-1}) \end{bmatrix} \quad (65)$$

with

$$\mathcal{H}(\hat{\mathbf{f}}_j) = \begin{bmatrix} \hat{f}[0,j] & \hat{f}[1,j] & \cdots & \hat{f}[p_1-1,j] \\ \hat{f}[1,j] & \hat{f}[2,j] & \cdots & \hat{f}[p_1,j] \\ \vdots & \vdots & \ddots & \vdots \\ \hat{f}[n_1-p_1,j] & \hat{f}[n_1-p_1+1,j] & \cdots & \hat{f}[n_1-1,j] \end{bmatrix} \in \mathbb{C}^{(n_1-p_1+1) \times p_1}, \quad (66)$$

and the annihilating filter vector is given by

$$\hat{\mathbf{h}} = \overline{\text{VEC}(\hat{H})}, \quad (67)$$

where the overline denotes an operator that reserves the order of a vector. Using this, we can construct an augmented matrix  $\mathcal{Y}$  in (52) from  $r$ -channels.

The augmented matrix structure  $\mathcal{H}(\hat{F})$  illustrated in Fig. 2(b) is similar to those of SAKE and LORAKS/P-LORAKS in Fig. 2(c) and (d), respectively, with the following differences. Compared to SAKE, ALOHA stacks the multi-coil Hankel matrices side by side. Unlike the SAKE and ALOHA, LORAKS uses 4-neighbors. However, these are negligible differences since the construction by SAKE is just a transpose of ALOHA and LORAKS could use different set of neighbours. Therefore, the main novelty of the proposed method is the k-space weighting before the Hankel structured matrix construction.

### B. Hankel structured matrix completion algorithm

In order to solve Eqs. (17), (32), (32), and (53), we employ an SVD-free structured rank minimization algorithm [35] with an initialization using the low-rank factorization model (LMaFit) algorithm [36]. This algorithm does not use the singular value decomposition (SVD), so the computational complexity can be significantly reduced. Similar approaches have been studied in previous researches [37], [38]. Specifically, the algorithm is based on the following observation [39]:

$$\|A\|_* = \min_{U,V:A=UV^H} \|U\|_F^2 + \|V\|_F^2 \quad . \quad (68)$$

Hence, (17) can be reformulated as the nuclear norm minimization problem under the matrix factorization constraint:

$$\begin{aligned} \min_{U,V:\mathcal{H}(\mathbf{m})=UV^H} \quad & \|U\|_F^2 + \|V\|_F^2 \\ \text{subject to} \quad & P_\Omega(\mathbf{m}) = P_\Omega(\hat{\mathbf{f}}), \end{aligned} \quad (69)$$

By combining the two constraints, we have the following cost function for an alternating direction method of multiplier (ADMM) step [40]:

$$L(U, V, \mathbf{m}, \Lambda) := \iota(\mathbf{m}) + \frac{1}{2} (\|U\|_F^2 + \|V\|_F^2) + \frac{\mu}{2} \|\mathcal{H}(\mathbf{m}) - UV^H + \Lambda\|_F^2 \quad (70)$$

where  $\iota(\mathbf{m})$  denotes an indicator function:

$$\iota(\mathbf{m}) = \begin{cases} 0, & \text{if } P_\Omega(\mathbf{m}) = P_\Omega(\hat{\mathbf{f}}) \\ \infty, & \text{otherwise} \end{cases} \quad .$$

One of the advantages of the ADMM formulation is that each subproblem is simply obtained from (70).

More specifically, we have

$$\mathbf{m}^{(n+1)} = \arg \min_{\mathbf{m}} \iota(\mathbf{m}) + \frac{\mu}{2} \|\mathcal{H}(\mathbf{m}) - U^{(n)}V^{(n)H} + \Lambda^{(n)}\|_F^2 \quad (71)$$

$$U^{(n+1)} = \arg \min_U \frac{1}{2} \|U\|_F^2 + \frac{\mu}{2} \|\mathcal{H}(\mathbf{m}^{(n+1)}) - UV^{(n)H} + \Lambda^{(n)}\|_F^2 \quad (72)$$

$$V^{(n+1)} = \arg \min_V \frac{1}{2} \|V\|_F^2 + \frac{\mu}{2} \|\mathcal{H}(\mathbf{m}^{(n+1)}) - U^{(n+1)}V^H + \Lambda^{(n)}\|_F^2 \quad (73)$$

$$\Lambda^{(n+1)} = \mathcal{Y}^{(n+1)} - U^{(n+1)}V^{(n+1)H} + \Lambda^{(n)} \quad (74)$$

It is easy to show that the first step can be reduced to

$$\mathbf{m}^{(n+1)} = P_{\Omega^c} \mathcal{H}^\dagger \left\{ U^{(n)}V^{(n)H} - \Lambda^{(n)} \right\} + P_\Omega(\hat{\mathbf{f}}), \quad (75)$$

where  $P_{\Omega^c}$  is a projection mapping on the set  $\Omega^c$  and  $\mathcal{H}^\dagger$  corresponds to the Penrose-Moore pseudo-inverse mapping from our block Hankel structure to a vector. Hence, the role of the pseudo-inverse is

taking the average value and putting it back to the original coordinate. Next, the subproblem for  $U$  and  $V$  can be easily calculated by taking the derivative with respect to each matrix, and we have

$$U^{(n+1)} = \mu \left( \mathcal{Y}^{(n+1)} + \Lambda^{(n)} \right) V^{(n)} \left( I + \mu V^{(n)H} V^{(n)} \right)^{-1} \quad (76)$$

$$V^{(n+1)} = \mu \left( \mathcal{Y}^{(n+1)} + \Lambda^{(n)} \right)^H U^{(n+1)} \left( I + \mu U^{(n+1)H} U^{(n+1)} \right)^{-1}. \quad (77)$$

Note that the computational complexity of our ADMM algorithm is dependent on the matrix inversion in (76) and (77), whose complexity is determined by the estimated rank of the Hankel matrix. Therefore, even though the Hankel matrix has large size, the estimated rank is much smaller, which significantly reduces overall complexity.

Now, for faster convergence, the remaining issue is how to initialize  $U$  and  $V$ . For this, we employ an algorithm called the low-rank factorization model (LMaFit) [36]. More specifically, for a low-rank matrix  $Z$ , LMaFit solves the following optimization problem:

$$\min_{U, V, Z} \frac{1}{2} \|UV^H - Z\|_F^2 \text{ subject to } P_I(Z) = P_I(\mathcal{H}(\hat{\mathbf{f}})) \quad (78)$$

and  $Z$  is initialized with  $\mathcal{H}(\hat{\mathbf{f}})$  and the index set  $I$  denotes the positions where the elements of  $\mathcal{H}(\hat{\mathbf{f}})$  are known. LMaFit solves a linear equation with respect to  $U$  and  $V$  to find their updates and relaxes the updates by taking the average between the previous iteration and the current iteration. Moreover, the rank estimation can be done automatically. LMaFit uses QR factorization instead of SVD, so it is also computationally efficient. A similar matrix factorisation algorithm was proposed in [37], [38]. Even though the problem (78) is non-convex due to the multiplication of  $U$  and  $V$ , the convergence of LMaFit to a stationary point was analyzed in detail [36]. However, the LMaFit alone cannot recover the block Hankel structure, which is the reason we use an ADMM step afterward to impose the structure.

We are aware that SAKE, LORAKS and P-LORAKS use non-convex formulation for low rank completion since they may work better than a convex formulation using the nuclear norm with a proper initialisation. However, the convex formulation (69) is necessary to arrive at the explicit sampling rate [30], which employed the dual certificate and golfing scheme by David Gross [28] for the nuclear norm minimization. Therefore, our approach also utilizes the nuclear norm minimization.

### C. Reconstruction Flow

As shown in Fig. 1, the generalized ALOHA framework is comprised with several major steps: pyramidal decomposition, k-space weighting, Hankel matrix formation, rank estimation, SVD-free low rank matrix completion, and k-space unweighting.

The pyramidal decomposition is performed as follows. In multi-slice MR data acquisition illustrated in Fig. 1(a), the  $k_x - k_y$  data matrix at the current scale only contains one-fourth of data around zero frequency from that of the previous scale. On the other hand, in the case of dynamic imaging shown in Fig. 1(b), the  $k - t$  data in the current scale contains a half of the data from that of the previous scale. In both cases, the estimated k-space data at the lower scale are used to initialize the low rank matrix completion algorithm at the current scale. This accelerates the convergence speed. Moreover, due to the additional chance of refining the estimates, more important k-space samples at the low frequency regions are refined furthermore compared to the high frequency k-space samples. Consequently, the overall computational burden of the low rank matrix completion algorithm is significantly reduced while the overall quality is still maintained.

The k-space weighting is performed using wavelets. Specifically, based on our discussions on maximally localized smoothing function, we use a Haar wavelet expansion whose spectrum is given by

$$\hat{\psi}_0(\omega) = \frac{i\omega}{2} \left( \frac{\sin \omega/4}{\omega/4} \right)^2 \exp\left(-i\frac{\omega}{2}\right). \quad (79)$$

The corresponding k-space weighting at the  $s$ -scale is given by

$$\hat{l}_s(\omega) = \frac{1}{\sqrt{2^s}} \frac{i2^s\omega}{2} \left( \frac{\sin 2^s\omega/4}{2^s\omega/4} \right)^2 e^{-i\frac{2^s\omega}{2}}.$$

Care needs to be taken when applying the weighting to 2D Fourier domain because there are two frequency variables  $(\omega_x, \omega_y)$ . One could use a separable weighting  $\hat{l}(\omega_x, \omega_y) = \hat{l}(\omega_x)\hat{l}(\omega_y)$ ; however, the resulting problem is that the missing k-space components along the frequency axis  $\omega_x = 0$  or  $\omega_y = 0$  cannot be recovered. Consequently, we applied the weighting sequentially along each axis, i.e. we solve (32) by applying  $\hat{l}(\omega_x)$  first, which is followed by solving (32) with  $\hat{l}(\omega_y)$ .

Finally, after the k-space interpolation, the k-space unweighting is done in k-space pixel-by-pixel by dividing the reconstructed value with (79). Note that (79) has zero value at the DC frequency. However, because we acquire the DC value as well as some of the low frequency k-space data, the problem of dividing by zero never happens.

Because LORAKS corresponds to the ALOHA without weighting and wavelet decomposition, we use LORAKS as a reference to answer why the proposed ALOHA framework has many advantages. The implementation of LORAKS was based on the source code available in the original author's homepage, which requires manual setting of estimated ranks. We chose the rank for LORAKS that gave the best reconstruction quality.

We used TITAN GTX graphic card for graphic processor unit (GPU) and i7-4770k CPU and the

codes were written in MATLAB 2015a (Mathwork, Natick). To accelerate the algorithm, most part of the MATLAB codes were implemented using Compute Unified Device Architecture (CUDA) for GPU.

#### *D. MR Acquisition and Reconstruction Parameters*

To assess the performance of ALOHA for single coil compressed sensing imaging, k-space raw data from an MR headscan was obtained with Siemens Verio 3T scanner using 2D SE sequence. The acquisition parameters were as follows: TR/TE = 4000/100ms,  $256 \times 256$  acquisition matrix, and six z-slices with 5mm slice thickness. The field-of-view (FOV) was  $240 \times 240\text{mm}^2$ , and the number of coils was four. To perform single coil reconstruction, we chose MR raw data from one coil out of the four coils.

A retrospective down-sampling mask was generated according to a two dimensional Gaussian distribution and the data at the central  $7 \times 7$  region around zero frequency were obtained additionally. This is equivalent to assume a 3D imaging scenario where the readout direction is fully sampled and the downsampling is done in the remaining 2-D phase encoding direction. Downsampling factors of six was used to generate sampling masks. The k-space weighting in (79) was used. The generalized ALOHA reconstruction was conducted using the following parameters: three levels of pyramidal decomposition, and decreasing LMaFit tolerance values ( $10^{-1}, 10^{-2}, 10^{-3}$ ) at each level of the pyramid. In addition, an initial rank estimate for LMaFit started with one and was refined automatically in an increasing sequence, the annihilating filter size was  $15 \times 15$ , and the ADMM parameter was  $\mu = 10^3$ . For the compressed sensing approach, we used two approach with the same data and the same sampling masks: (1) the sparsity in wavelet domain (which we denote  $l_1$ -wavelet) [3], and (2) the split Bregman method for the total variation [41]. In case of  $l_1$ -wavelet approach, we implemented an ADMM algorithm using wavelet domain sparsity. In addition, for comparison with the existing state-of-the art approach using Hankel structured matrix completion algorithm, LORAKS was compared. In particular, C-based LORAKS was chosen because it exploits the image domain sparsity. The parameters for the  $l_1$ -wavelet and TV approaches were optimized to have the best performance in terms of the normalized mean square error (NMSE), which is defined by  $\text{NMSE}(\mathbf{x}) = \|\mathbf{x} - \mathbf{y}\|_2^2 / \|\mathbf{y}\|_2^2$ , where  $\mathbf{x}$  and  $\mathbf{y}$  denote the reconstructed and the ground-truth images, respectively. The LORAKS parameters were chosen manually to give the best reconstruction quality.

To evaluate the performance of ALOHA in static parallel imaging, the same brain data was used. Retrospectively undersampled 2-D k-space data at the acceleration factor of eight were obtained according to a two dimensional Gaussian distraction in addition to the  $7 \times 7$  central region around zero frequency. The data from 4 receiver coils were used. For comparison, we used the identical data and sampling masks

for SAKE [16], and SAKE with ESPIRiT [42]. Note that GRAPPA [13] requires ACS lines, so with the additional 50 samples along ACS, the effective downsampling ratio was 4.785, which is not good as the eight time acceleration in other algorithms. SAKE and SAKE with ESPIRiT are both low rank matrix completion algorithms for Hankel structured matrix collected from the whole k-space data. However, SAKE with ESPIRiT reduces the computational burden of the original SAKE by performing low rank matrix completion only for the  $65 \times 65$  central region with  $7 \times 7$  filter, after which coil sensitivities are estimated using the reconstruction data. The estimated coil sensitivities are used to estimate the remaining k-space missing data through ESPIRiT [42]. The parameters for SAKE and SAKE with ESPIRiT were chosen such that they provided the best reconstruction results. The parameters for the generalized ALOHA are as follows: three levels of pyramidal decomposition with decreasing LMaFit tolerances ( $10^{-1}$ ,  $10^{-2}$ ,  $10^{-3}$ ), and  $7 \times 7$  annihilating filter. The same LMaFit rank estimation strategy and ADMM parameter used for single coil experiments were employed. We generated the square root of sum of squares (SSoS) image from multi-coil reconstructions.

We also validated the performance of ALOHA for accelerated dynamic cardiac data in the k-t domain. A cardiac cine data set was acquired using a 3T whole-body MRI scanner (Siemens; Tim Trio) equipped with a 32-element cardiac coil array. The acquisition sequence was bSSFP and prospective cardiac gating was used. The imaging parameters were as follows: FOV=  $300 \times 300 \text{mm}^2$ , acquisition matrix size=  $128 \times 128$ , TE/TR = 1.37/2.7ms, receiver bandwidth = 1184Hz/pixel, and flip angle =  $40^\circ$ . The number of cardiac phases was 23 and the temporal resolution was 43.2ms. The k-t space samples including four lines around zero frequency were retrospectively obtained at the reduction factor of eight according to a Gaussian distribution. For comparison, k-t FOCUSS [7], LORAKS [17], and SAKE [16] was used. In case of LORAKS (single coil) and SAKE (multi coil), these algorithms were applied to k-t domain for dynamic reconstruction. The parameters in k-t FOCUSS, LORAKS, and SAKE, were selected to give the best NMSE values. For the generalized ALOHA in single coil data, the following parameters were used: three level of pyramidal decomposition only along the phase encoding direction, decreasing LMaFit tolerances ( $10^{-1}$ ,  $10^{-2}$ ,  $10^{-3}$ ) at each scale, and  $17 \times 5$  annihilating filter. The same LMaFit rank estimation strategy and ADMM parameter was  $\mu = 10$ . The k-space weighting in Eq. (79) was applied only along the phase encoding direction.

Next, we investigated the synergetic improvement of dynamic imaging from multi-channel acquisition. Four representative coils out of 32 were used. The reason we chose only four coils was to verify that the generalised ALOHA can maximally exploit the multi-channel diversity even with the small number

of coils. The four coils were chosen such that it covers every area of images. The same four coils were used for all algorithms for fair comparison. In the generalized ALOHA, the annihilating filter size was  $7 \times 7$ . The same LMaFit rank estimation strategy and ADMM parameter used before were employed. After the reconstructions of k-space samples, the inverse Fourier transform was applied, and the SSoS images were obtained by combining the reconstructed images.

## IV. RESULTS

### A. Static MR experiments

Reconstructed results from a single coil brain data are shown in Fig. 3 with the NMSE values. From the NMSE values, we observed that the performance ALOHA was quantitatively superior to the performance of  $l_1$ -wavelet and TV based compressed sensing approach. The reconstruction results by ALOHA has less perceivable distortion compared to those of  $l_1$ -wavelet and TV approaches. This can be easily observed from the difference images in the second and the fourth rows of Fig. 3. In the case of  $l_1$ -wavelets and TV, structural distortion around the image edges was easily recognizable. In the last row of Fig. 3, the edges were reconstructed accurately by ALOHA. On the other hand, the contrast between grey matters and white matters in  $l_1$ -wavelets and TV reconstruction were significantly distorted compared with that of ALOHA. The LORAKS reconstruction was better than that of  $l_1$ -wavelets and TV reconstruction, but there were still remaining errors around the edges and the NMSE value was significantly higher than that of ALOHA.

Next we compared our parallel imaging results with those of the existing approaches for the same brain data set. The NMSE results in Fig. 4 showed that ALOHA was most accurate. From the difference images at the second row of Fig. 4, we observed that proposed method provided reconstruction results more accurately than other algorithms. In SAKE, the structures were distorted around the inner skull and the boundaries of tissues. In SAKE with ESPIRiT, overall reconstruction errors were higher than those from ALOHA and there were still remaining errors around the skull. The reconstruction time was 22.2sec with our preliminary GPU implementation of ALOHA, which attained a speed-up factor of 5 compared to CPU implementation. On the other hand, the computational time for MATLAB version of GRAPPA, SAKE, and SAKE+ESPIRiT were 9s, 320.4s, and 21.6s, respectively.

### B. Dynamic MR experiments

Using the sub-sampled k-space data at the acceleration factor of eight, the average NMSE values of k-t FOCUS, LORAKS, and ALOHA, were  $1.616 \times 10^{-2}$ ,  $1.363 \times 10^{-2}$ , and,  $1.151 \times 10^{-2}$ , respectively.

The sub-sampled data was collected according to a Gaussian distribution and included the four center lines around zero frequency. The average NMSE values were calculated using all temporal frames. These results confirmed that the proposed method outperformed k-t FOCUSS and LORAKS. As shown in Fig. 5(a), the temporal profile (indicated as a broken purple line) of the proposed reconstruction provided more accurate structures especially at systole phase that were comparable to the true one, whereas the temporal variation in the k-t FOCUSS and LORAKS reconstruction became smoother and more blurry along the temporal dimension.

The NMSE values of the parallel dynamic imaging results from k-t FOCUSS, SAKE, and the proposed method using four coil k-space data were  $8.75 \times 10^{-3}$ ,  $4.983 \times 10^{-3}$  and  $3.436 \times 10^{-3}$ , respectively, which quantitatively showed that the proposed method outperformed k-t FOCUSS and SAKE. Reduced residual artifacts were perceivable in the ALOHA difference images in Fig. 5(b). Moreover, the temporal profiles of the proposed reconstruction showed more accurate structures which were comparable to the true one, whereas the dynamic slice profile from k-t FOCUSS and SAKE showed smoother and more blurry transition. In particular, the proposed algorithm resulted in more accurate reconstructions of dynamic changes at the heart wall in systole phase as shown in Fig. 5(b).

### C. Effects of k-space weighting

Figures 6(a)(b) illustrates the effects of TV and wavelet weighting schemes. Figs. 6(a)(b) show the corresponding images when a k-space weighting  $\hat{l}(\omega_y)$  is applied in the  $\omega_y$  direction. We can confirm that k-space weighting schemes enhanced the image edges. In order to identify the best k-space weighting scheme that promotes sparsity, we plotted the normalized singular value distribution of Hankel matrices from the  $1/4 \times 1/4$  central k-space region. The reason we chose the central region is to avoid the noise amplification effect at higher frequency regions that can deteriorate our analysis. As shown in Fig. 6(a)(b), the singular value spectrum of the Hankel structured matrix with non-uniform weights decayed much faster than the original signals. In addition, because these two weighting schemes are derived from the same signal model (27), there are negligible differences between the TV and Haar wavelet weighting schemes. However, when we perform reconstruction with two approach, we observed perceivable differences. Specifically, the difference images from ALOHA reconstruction with the TV operator weighting and Haar wavelet weightings in Figs. 6(a)(b) showed that the reconstructed images with Haar wavelet showed the best NMSE and visual quality in both single and multi-coil data. This result confirmed that, in spite of the same signal model (27), the wavelet approach is more robust to noise and model mismatch as observed in the theory of sparse stochastic processes [32], [33]

## V. DISCUSSION

In order to show the importance of the pyramidal decomposition, Fig. 7 plots the computational time versus NMSE values of single coil brain data by changing the number of decomposition levels. As discussed before, the maximum decomposition level is determined by the acquired low frequency components and the annihilating filter size. In this data set, k-space dimension was  $256 \times 256$  and the annihilating filter size was  $15 \times 15$ , and  $7 \times 7$  k-space data around zero frequency were acquired. By converting the Hankel matrix dimension in (65) for the  $s$ -scale, the number of rows should not be smaller than the number of columns; so we should impose constraints

$$n_1/2^s - p_1 + 1 = 256/2^s - 15 + 1 \geq 15,$$

where  $s$  is the scale. This provides  $s \leq 3$ , and the maximum scale becomes 3. Our experimental data showed that the performance gain increases as a scale increases; however, at the last decomposition level, the performance improvement was negligible. Therefore, the maximum scale was determined as the maximum minus one. Because we should include  $s = 0$ , the total number of decomposition is set to the maximum value.

The other important reconstruction parameters include the size of the annihilating filter, the number of iterations, and tolerances used in LMaFit algorithm. Recall that the annihilating filter size corresponds to the matrix pencil size in sensor array signal processing [31], and it should be set larger than the sparsity level of the transform coefficients. In fact, by considering the expression of  $c_s$  in (19), the optimal annihilating filter size for 2D data is  $n_1/2 \times m_1/2$ , where  $n_1 \times m_1$  denotes the full k-space data size. However, such large annihilating filter size introduces significant computational burden, so we tried to reduce the filter size as long as the image quality is not degraded. Based on extensive experiments, we found that in single coil image, the filter size should be sufficiently large as the annihilating filter size is solely determined by the sparsity level. In parallel imaging, there exist additional annihilating filters from the intercoil relationship, so the annihilating filter size can be set smaller than that of a single coil imaging.

Finally, the tolerance level for LMaFit, which corresponds to the fitting accuracy, plays key role in determining the initial rank estimate. The initial rank estimate need not be close to the exact rank, but it was used to define the dimension of  $U$  and  $V$  in ADMM. We found that the tolerance level could be determined by considering different noise contributions in k-space data. Specifically, higher frequency components are usually contaminated by higher level of noises compared to the low frequency k-space

data, so the LMaFit fitting accuracy need not be enforced strictly. This was the case when LMaFit was applied at a lower scale, since high frequency k-space data are more weighted and noises were boosted. On the other hand, more accurate fitting is required for higher scale data where the lower frequency k-space data are more weighted. Consequently, we chose decreasing values of tolerances per scale for in-vivo experiments.

We have also applied the proposed method for various applications such as T1 and T2 parameter mapping [43], which consistently showed that the proposed method significantly outperformed the existing state-of-the art approaches. More details can be found in our companion paper [43].

## VI. CONCLUSION

In this paper, we proposed a general framework for annihilating filter based low-rank Hankel matrix approach (ALOHA) for static and dynamic MRI inspired by recent calibration-free k-space methods such as SAKE and LORAKS/P-LORAKS. We confirmed the existing observation that the low rankness of the Hankel structured matrix in SAKE and LORAKS/P-LORAKS are derived from inter-coil correlation and image domain sparsity, and revealed that the required number of k-space data is given by  $ck \log^4 n_1$ , where  $k$  denotes the sparsity level. Because natural images can be much more effectively sparsified in the transform domains, we generalized the idea to include signals that can be sparsified in the transform domains. Our analysis showed that the transform domain sparsity can be equivalently represented as low-rank Hankel structured matrix in the weighted k-space domain, whose weighting function is determined solely by the transform, not by the data. Another significant discovery was that when signals are effectively sparsified in dyadic wavelet transform, the corresponding low rank Hankel matrix completion problem can be equivalently represented with a pyramidal decomposition, which significantly reduces the overall computational complexity. Moreover, unlike other weighting schemes applied at single scale, the pyramidal decomposition using wavelets provided best reconstruction quality that was less sensitive to noise. For parallel imaging data, we verified that by stacking Hankel matrix from each coil side by side, we may fully exploit the coil sensitivity diversity thanks to its relationship to MMV compressed sensing.

Reconstruction results from single coil static MR imaging confirmed that the proposed method outperformed the existing compressed sensing framework with TV regularization. We further demonstrated superior performance of the proposed method in static parallel MR imaging even without calibration data. Furthermore, the algorithm was successfully extended to dynamic accelerated MRI along k-t domain with

both single coil and multi coil dynamic MR data. Therefore, we concluded that the proposed algorithm was very effective in unifying the compressed sensing and parallel MRI.

## VII. ACKNOWLEDGMENT

This work was supported by Korea Science and Engineering Foundation under Grant NRF-2014R1A2A1A11052491.

## APPENDIX

Spectral domain uniform sampling at the distance of  $2\pi/\tau$  generates the periodic stream of Diracs:

$$f(x) = \sum_{j=0}^{k-1} c_j \sum_{n \in \mathbb{Z}} \delta(x - x_j - n\tau)$$

which can be represented as

$$\begin{aligned} f(x) &= \sum_{j=0}^{k-1} c_j \frac{1}{\tau} \sum_{n \in \mathbb{Z}} e^{i(2\pi n(x-x_j)/\tau)} \\ &= \sum_{n \in \mathbb{Z}} \hat{f}[n] e^{i2\pi n x/\tau} \end{aligned}$$

where the Fourier series coefficient  $\hat{f}[n]$  is given by

$$\hat{f}[n] = \frac{1}{\tau} \sum_{j=0}^{k-1} c_j e^{-i2\pi x_j n/\tau}. \quad (80)$$

If we construct a filter

$$h(z) = \sum_{n=0}^k \hat{h}[n] z^{-n} = \prod_{j=0}^{k-1} (1 - e^{-i2\pi x_j/\tau} z^{-1}), \quad (81)$$

then we can show that it annihilates the signal  $\hat{f}[n]$  because

$$\begin{aligned} (\hat{h} * \hat{f})[n] &= \sum_{l=0}^k \hat{h}[l] \hat{f}[n-l] \\ &= \sum_{l=0}^k \sum_{j=0}^{k-1} c_j \hat{h}[l] u_j^{n-l} \\ &= \sum_{j=0}^{k-1} c_j \underbrace{\left( \sum_{l=0}^k \hat{h}[l] u_j^{-l} \right)}_{\hat{h}(u_j)} u_j^n = 0 \end{aligned} \quad (82)$$

where  $u_j = e^{-i2\pi x_j/\tau}$ .

## REFERENCES

- [1] D. L. Donoho, "Compressed sensing," *IEEE Trans. Inf. Theory*, vol. 52, no. 4, pp. 1289–1306, 2006.
- [2] E. J. Candès, J. Romberg, and T. Tao, "Robust uncertainty principles: Exact signal reconstruction from highly incomplete frequency information," *IEEE Trans. Inf. Theory*, vol. 52, no. 2, pp. 489–509, 2006.

- [3] M. Lustig, D. Donoho, and J. M. Pauly, "Sparse MRI: The application of compressed sensing for rapid MR imaging," *Magn. Reson. Med.*, vol. 58, no. 6, pp. 1182–1195, 2007.
- [4] D. Liang, B. Liu, J. Wang, and L. Ying, "Accelerating SENSE using compressed sensing," *Magn. Reson. Med.*, vol. 62, no. 6, pp. 1574–1584, 2009.
- [5] J. P. Haldar, D. Hernando, and Z.-P. Liang, "Compressed-sensing MRI with random encoding," *IEEE Trans. Med. Imag.*, vol. 30, no. 4, pp. 893–903, 2011.
- [6] S. S. Vasanaawala, M. T. Alley, B. A. Hargreaves, R. A. Barth, J. M. Pauly, and M. Lustig, "Improved pediatric MR imaging with compressed sensing 1," *Radiology*, vol. 256, no. 2, pp. 607–616, 2010.
- [7] H. Jung, K. Sung, K. S. Nayak, E. Y. Kim, and J. C. Ye, "k-t FOCUSS: A general compressed sensing framework for high resolution dynamic MRI," *Magn. Reson. Med.*, vol. 61, no. 1, pp. 103–116, 2009.
- [8] H. Jung, J. Park, J. Yoo, and J. C. Ye, "Radial k-t FOCUSS for high-resolution cardiac cine MRI," *Magn. Reson. Med.*, vol. 63, no. 1, pp. 68–78, 2010.
- [9] H. Yoon, K. Kim, D. Kim, Y. Bresler, and J. Ye, "Motion adaptive patch-based low-rank approach for compressed sensing cardiac cine MRI," *IEEE Trans. Med. Imag.*, vol. 33, no. 11, pp. 2069–2085, Nov 2014.
- [10] S. G. Lingala, Y. Hu, E. DiBella, and M. Jacob, "Accelerated dynamic MRI exploiting sparsity and low-rank structure: kt SLR," *IEEE Trans. Med. Imag.*, vol. 30, no. 5, pp. 1042–1054, 2011.
- [11] T. Çukur, M. Lustig, and D. G. Nishimura, "Improving non-contrast-enhanced steady-state free precession angiography with compressed sensing," *Magn. Reson. Med.*, vol. 61, no. 5, pp. 1122–1131, 2009.
- [12] K. P. Pruessmann, M. Weiger, M. B. Scheidegger, P. Boesiger *et al.*, "SENSE: sensitivity encoding for fast MRI," *Magn. Reson. Med.*, vol. 42, no. 5, pp. 952–962, 1999.
- [13] M. A. Griswold, P. M. Jakob, R. M. Heidemann, M. Nittka, V. Jellus, J. Wang, B. Kiefer, and A. Haase, "Generalized autocalibrating partially parallel acquisitions (GRAPPA)," *Magn. Reson. Med.*, vol. 47, no. 6, pp. 1202–1210, 2002.
- [14] K. P. Pruessmann, "Encoding and reconstruction in parallel MRI," *NMR in Biomedicine*, vol. 19, no. 3, pp. 288–299, 2006.
- [15] M. Lustig and J. M. Pauly, "SPIRiT: Iterative self-consistent parallel imaging reconstruction from arbitrary k-space," *Magn. Reson. Med.*, vol. 64, no. 2, pp. 457–471, 2010.
- [16] P. J. Shin, P. E. Larson, M. A. Ohliger, M. Elad, J. M. Pauly, D. B. Vigneron, and M. Lustig, "Calibrationless parallel imaging reconstruction based on structured low-rank matrix completion," *Magn. Reson. Med.*, vol. 72, no. 4, pp. 959–970, 2014.
- [17] J. Haldar, "Low-rank modeling of local  $k$ -space neighborhoods (LORAKS) for constrained MRI," *IEEE Trans. Med. Imag.*, vol. 33, no. 3, pp. 668–681, March 2014.
- [18] J. P. Haldar and J. Zhuo, "P-LORAKS: Low-rank modeling of local  $k$ -space neighborhoods with parallel imaging data," *Magn. Reson. Med.*, 2015.
- [19] M. Vetterli, P. Marziliano, and T. Blu, "Sampling signals with finite rate of innovation," *IEEE Trans. Signal Process.*, vol. 50, no. 6, pp. 1417–1428, 2002.
- [20] P. L. Dragotti, M. Vetterli, and T. Blu, "Sampling moments and reconstructing signals of finite rate of innovation: Shannon meets Strang-Fix," *IEEE Trans. Signal Process.*, vol. 55, no. 5, pp. 1741–1757, 2007.
- [21] I. Maravic and M. Vetterli, "Sampling and reconstruction of signals with finite rate of innovation in the presence of noise," *IEEE Trans. Signal Process.*, vol. 53, no. 8, pp. 2788–2805, 2005.
- [22] J. M. Kim, O. K. Lee, and J. C. Ye, "Compressive MUSIC: revisiting the link between compressive sensing and array signal processing," *IEEE Trans. Inf. Theory*, vol. 58, no. 1, pp. 278–301, 2012.
- [23] K. Lee, Y. Bresler, and M. Junge, "Subspace methods for joint sparse recovery," *IEEE Trans. Inf. Theory*, vol. 58, no. 6, pp. 3613–3641, 2012.
- [24] M. E. Davies and Y. C. Eldar, "Rank awareness in joint sparse recovery," *IEEE Trans. Inf. Theory*, vol. 58, no. 2, pp. 1135–1146, 2012.
- [25] E. J. Candès and B. Recht, "Exact matrix completion via convex optimization," *Found. Comput. Math.*, vol. 9, no. 6, pp. 717–772, 2009.
- [26] J.-F. Cai, E. J. Candès, and Z. Shen, "A singular value thresholding algorithm for matrix completion," *SIAM Journal on Optimization*, vol. 20, no. 4, pp. 1956–1982, 2010.
- [27] E. J. Candès and T. Tao, "The power of convex relaxation: Near-optimal matrix completion," *IEEE Trans. Inf. Theory*, vol. 56, no. 5, pp. 2053–2080, 2010.
- [28] D. Gross, "Recovering low-rank matrices from few coefficients in any basis," *IEEE Trans. Inf. Theory*, vol. 57, no. 3, pp. 1548–1566, 2011.
- [29] R. H. Keshavan, A. Montanari, and S. Oh, "Matrix completion from a few entries," *IEEE Trans. Inf. Theory*, vol. 56, no. 6, pp. 2980–2998, 2010.
- [30] Y. Chen and Y. Chi, "Robust spectral compressed sensing via structured matrix completion," *IEEE Trans. Inf. Theory*, vol. 60, no. 10, pp. 6576 – 6601, 2014.
- [31] Y. Hua and T. K. Sarkar, "Matrix pencil method for estimating parameters of exponentially damped/undamped sinusoids in noise," *IEEE Trans. Acoust., Speech, Signal Process.*, vol. 38, no. 5, pp. 814–824, 1990.
- [32] M. Unser, P. D. Tafti, and Q. Sun, "A unified formulation of Gaussian versus sparse stochastic processes—Part I: Continuous-domain theory," *IEEE Trans. Inf. Theory*, vol. 60, no. 3, pp. 1945–1962, 2014.

- [33] M. Unser, P. Tafti, A. Amini, and H. Kirshner, "A unified formulation of Gaussian versus sparse stochastic processes—Part II: Discrete-domain theory," *IEEE Trans. Inf. Theory*, vol. 60, no. 5, pp. 3036–3051, 2014.
- [34] J. P. Haldar and Z.-P. Liang, "Low-rank approximations for dynamic imaging," in *2011 IEEE International Symposium on Biomedical Imaging: From Nano to Macro*. IEEE, 2011, pp. 1052–1055.
- [35] M. Signoretto, V. Cevher, and J. A. Suykens, "An SVD-free approach to a class of structured low rank matrix optimization problems with application to system identification," in *IEEE Conf. on Decision and Control*, 2013.
- [36] Z. Wen, W. Yin, and Y. Zhang, "Solving a low-rank factorization model for matrix completion by a nonlinear successive over-relaxation algorithm," *Math. Prog. Comp.*, vol. 4, no. 4, pp. 333–361, 2012.
- [37] J. P. Haldar and Z.-P. Liang, "Spatiotemporal imaging with partially separable functions: A matrix recovery approach," in *2010 IEEE International Symposium on Biomedical Imaging: From Nano to Macro*. IEEE, 2010, pp. 716–719.
- [38] S. G. Lingala and M. Jacob, "Blind compressive sensing dynamic mri," *IEEE Trans. Med. Imag.*, vol. 32, no. 6, pp. 1132–1145, 2013.
- [39] N. Srebro, "Learning with matrix factorizations," Ph.D. dissertation, Dept. of Elect. Eng. and Comput. Sci., MIT, MA, 2004.
- [40] S. Boyd, N. Parikh, E. Chu, B. Peleato, and J. Eckstein, "Distributed optimization and statistical learning via the alternating direction method of multipliers," *Found. Trends in Mach. Learn.*, vol. 3, no. 1, pp. 1–122, 2011.
- [41] T. Goldstein and S. Osher, "The split Bregman method for L1-regularized problems," *SIAM J. Imaging Sci.*, vol. 2, no. 2, pp. 323–343, 2009.
- [42] M. Uecker, P. Lai, M. J. Murphy, P. Virtue, M. Elad, J. M. Pauly, S. S. Vasanawala, and M. Lustig, "ESPIRiT—an eigenvalue approach to autocalibrating parallel MRI: Where SENSE meets GRAPPA," *Magn. Reson. Med.*, vol. 71, no. 3, pp. 990–1001, 2014.
- [43] D. Lee, K. H. Jin, E.-Y. Kim, S. Park, and J. C. Ye, "Acceleration of MR parameter mapping using annihilating filter-based low rank Hankel matrix (ALOHA)," *Magnetic Resonance in Medicine (submitted)*, 2015.

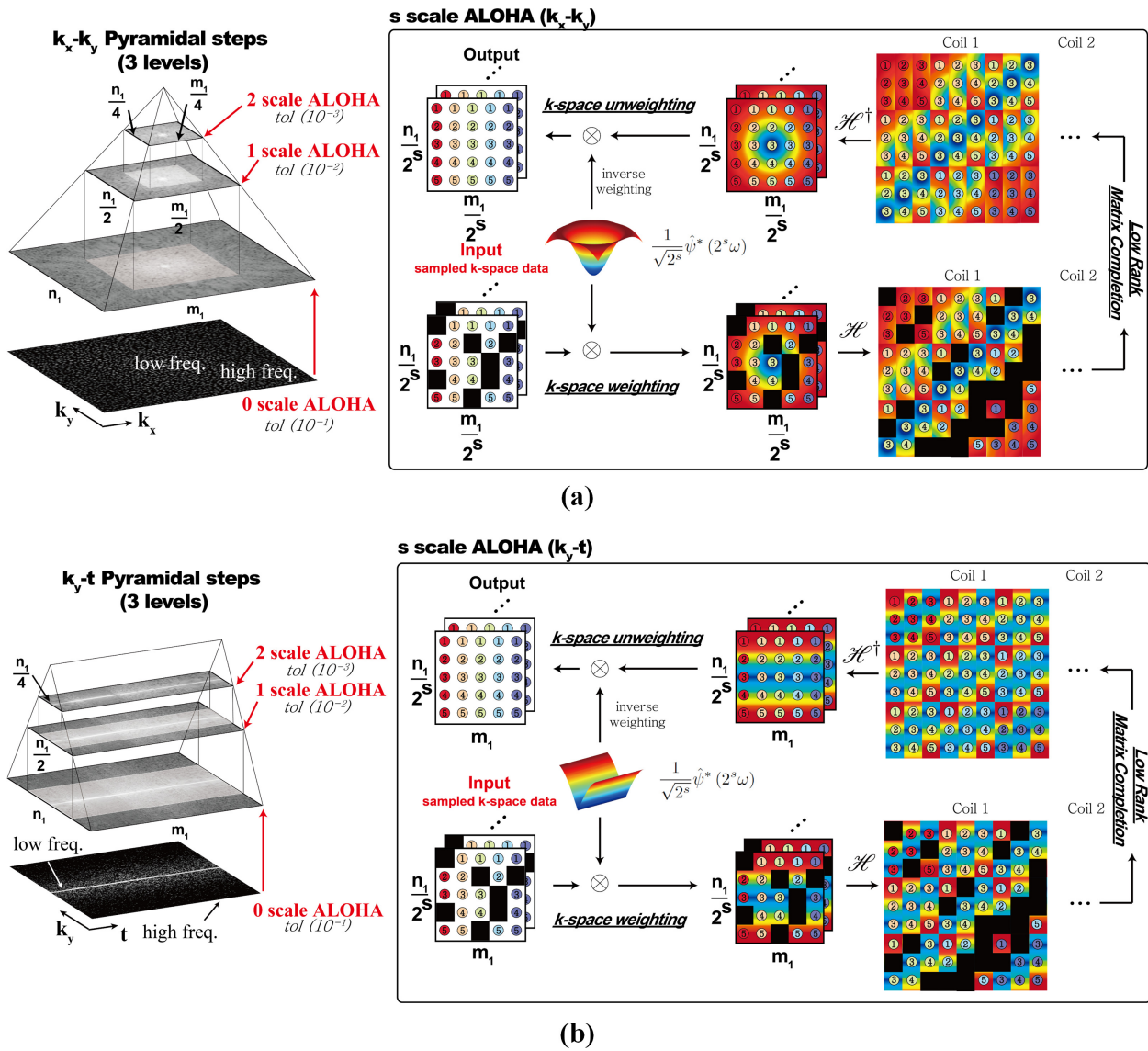


Fig. 1: Generalized ALOHA with dyadic wavelet transform from (a)  $k_x$ - $k_y$  and (b)  $k - t$  domain subsampled data, respectively.

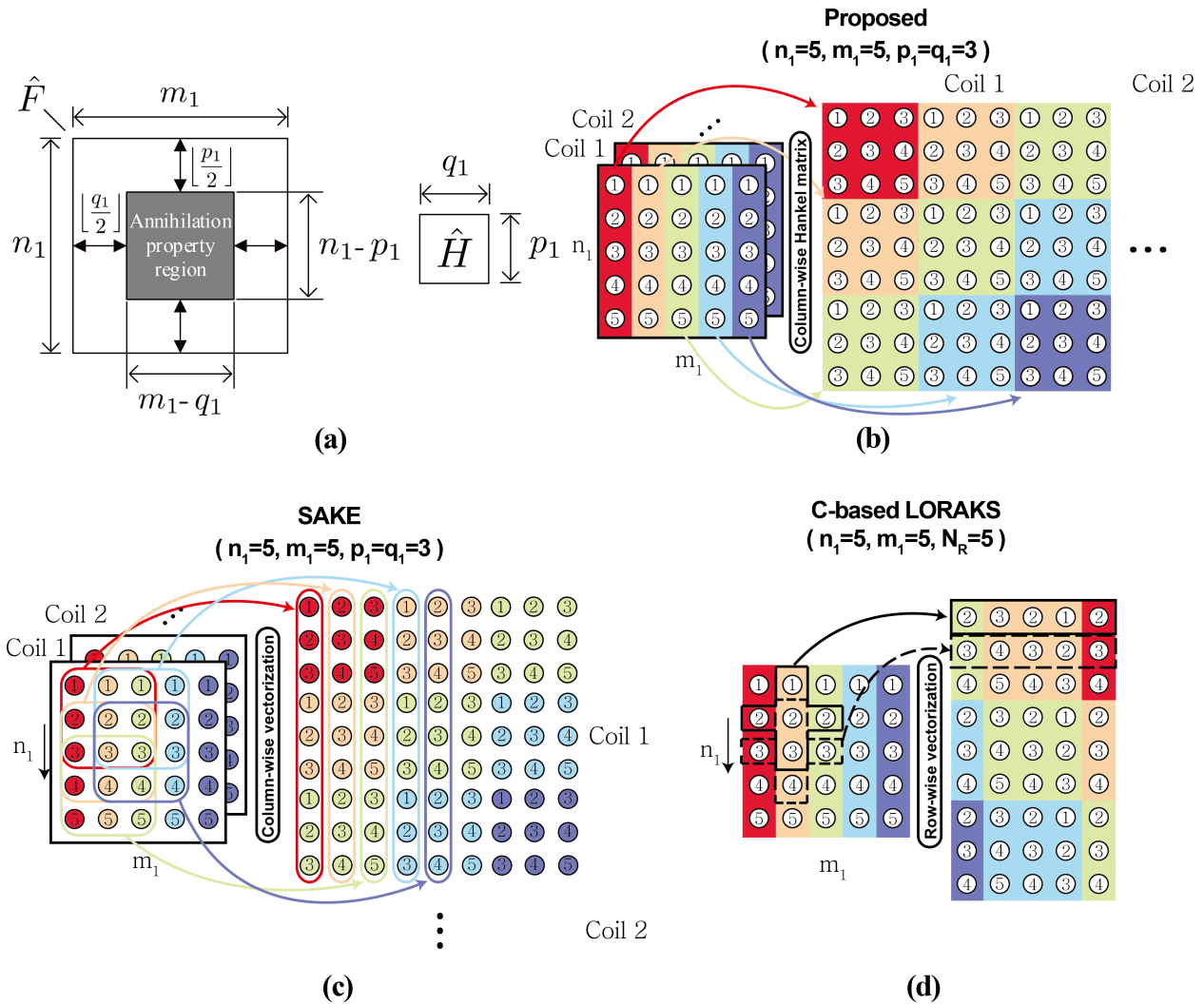


Fig. 2: (a) A boundary removed region where annihilation property holds. Various ways of constructing block Hankel matrices: (b) ALOHA, (c) SAKE, and (d) LORAKS. In (d),  $N_R$  denotes the number of neighborhood pixels.

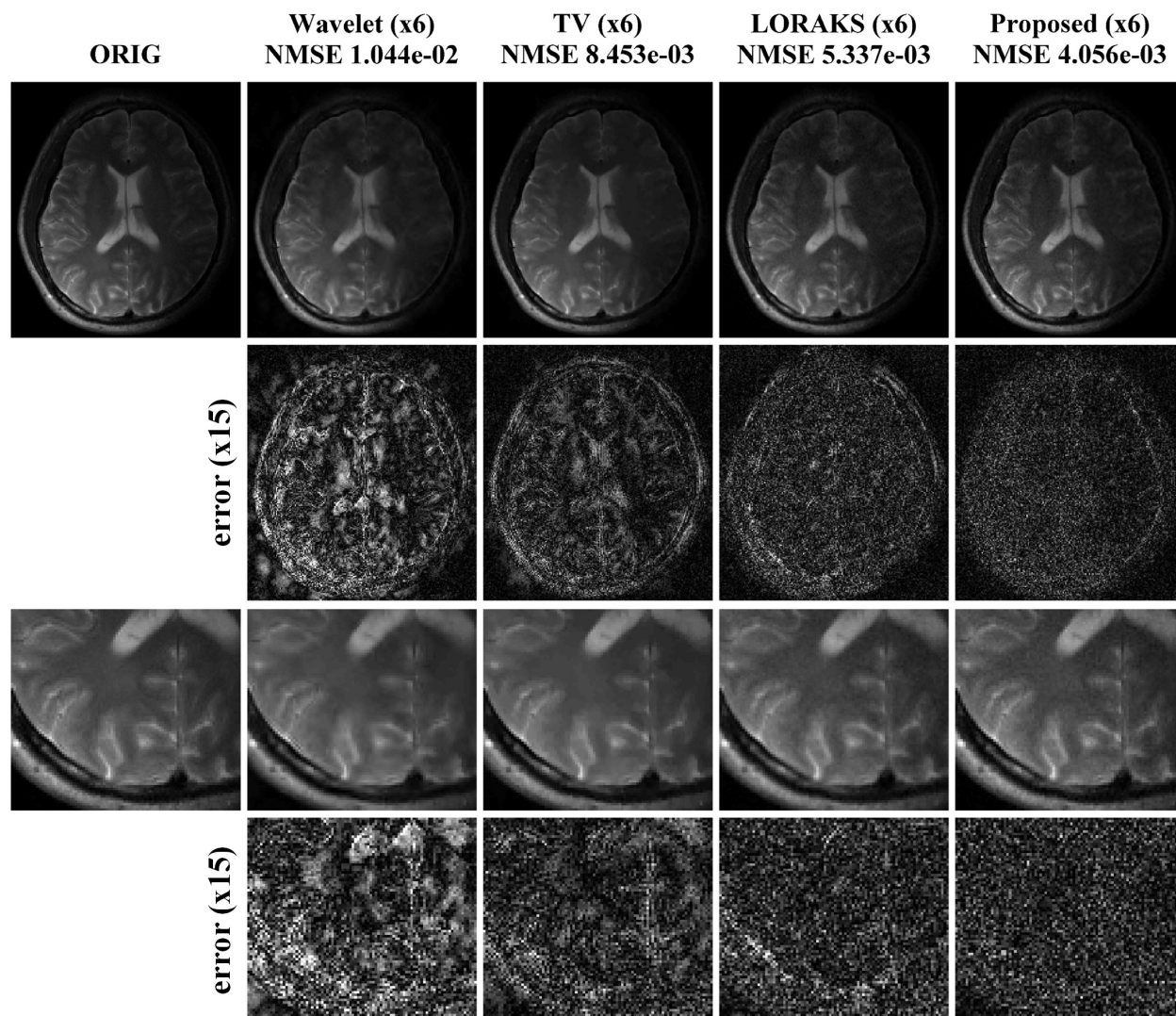


Fig. 3: Comparison with  $l_1$ -wavelet compressed sensing, TV compressed sensing, LORAKS, and the proposed method at 6 fold acceleration factors. The data was acquired from a single channel coil. The first row shows reconstructed images, and the second row shows difference images between the ground-truth and the reconstructions, and the third row shows the magnified views of distorted regions in the reconstructed images. The last row shows the difference images in the magnified views.

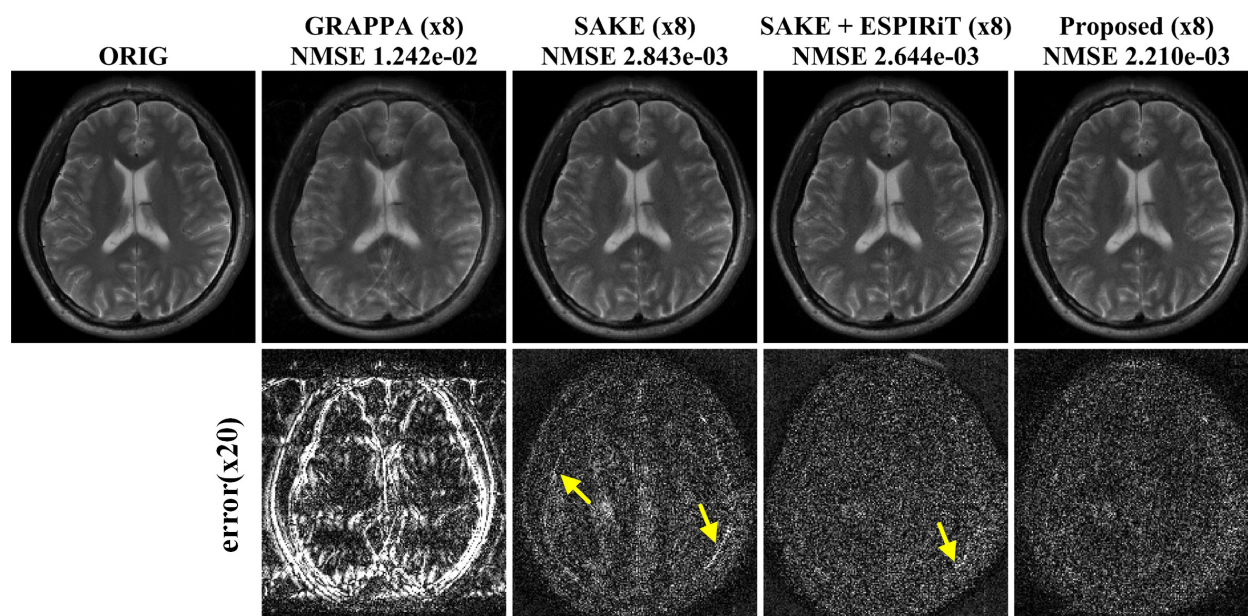
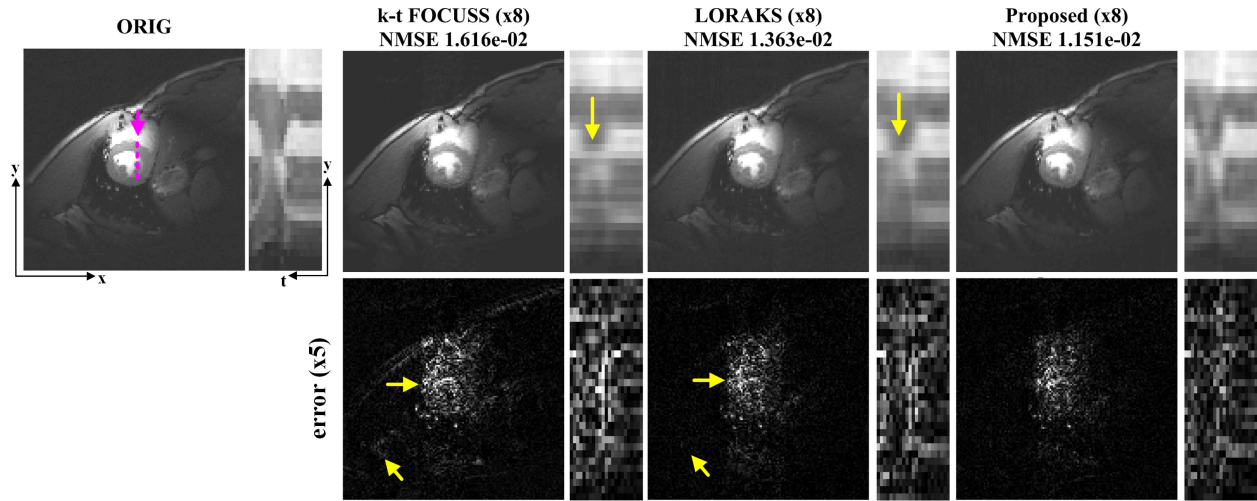
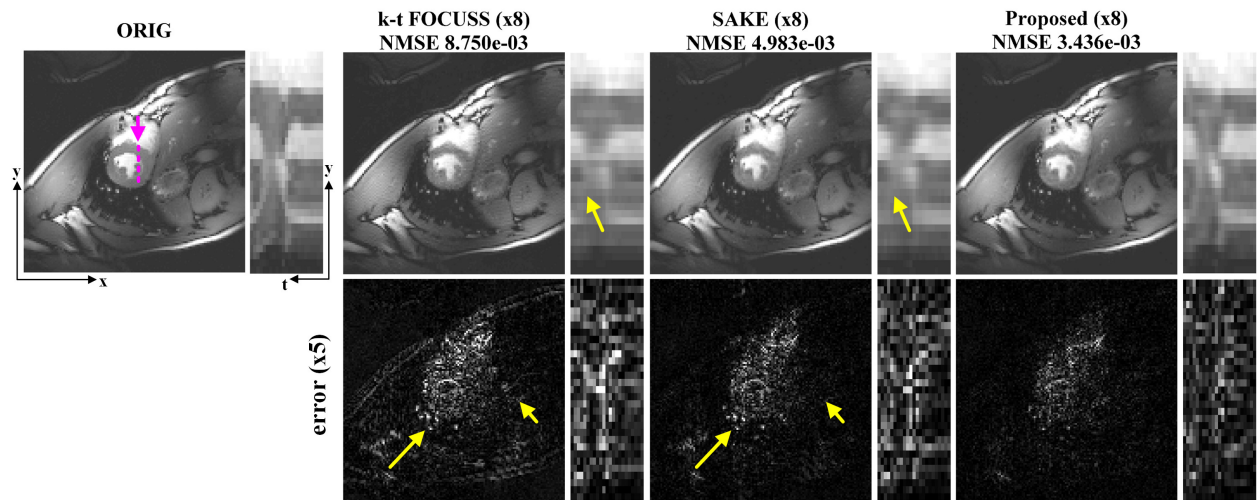


Fig. 4: Parallel imaging results using GRAPPA, SAKE, SAKE with ESPIRiT and the proposed method at 8 fold acceleration. The second row shows the difference images. Areas with systematic artefacts are indicated by yellow arrows.



(a) Single coil reconstruction results



(b) Parallel imaging results from 4 coils

Fig. 5: Reconstruction results from 8 fold accelerated k-space data using (a) single coil and (b) four coils data set. Purple lines denote the regions corresponding to y-t cross sections that are magnified along temporal axis. The second rows in both (a) and (b) show the difference images between the ground-truth and the reconstructions.

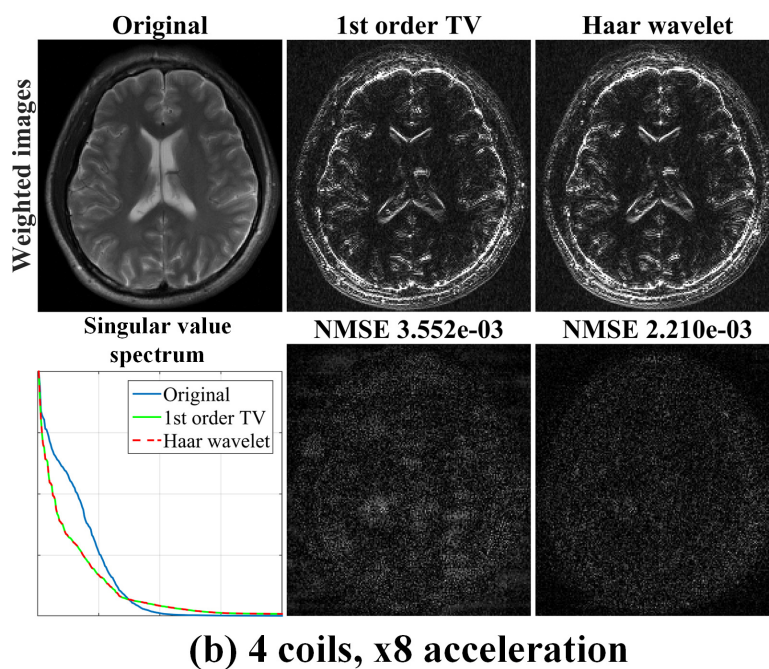
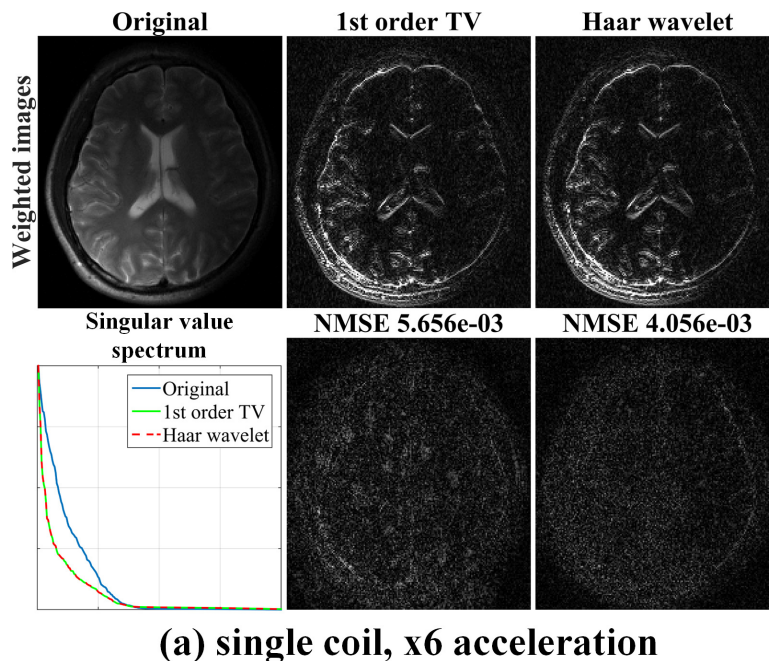


Fig. 6: Weighted images using the TV operator weighting and Haar wavelet weightings (1st order TV, and Haar wavelet) are shown in the first rows at (a)(b). In the second rows, the first graph shows singular value distribution of weighted Hankel matrices from the  $1/4 \times 1/4$  central k-space region. The last two images in the second rows show the residual images between the ground-truth and reconstructions. (a) is from single coil brain data, and (b) is from multi-coil brain data from 4 coils.

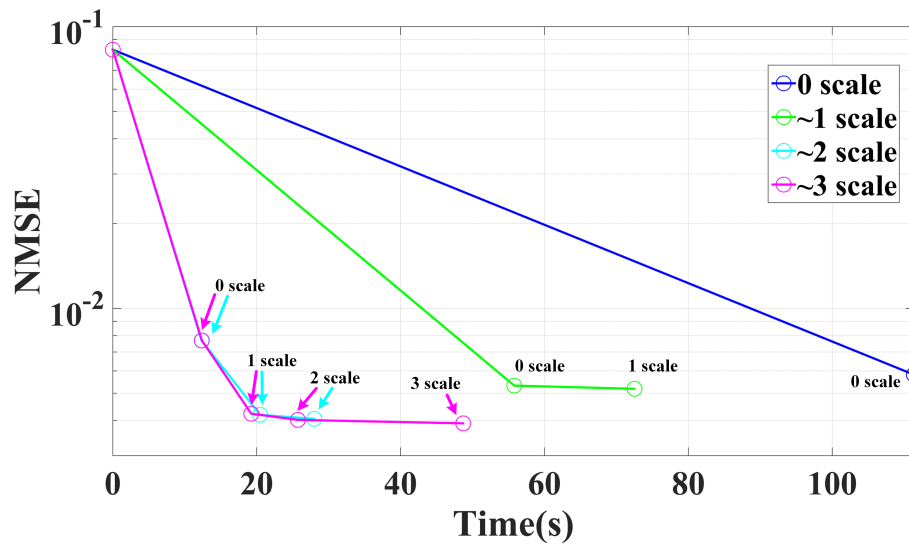


Fig. 7: Reconstruction NMSE values with respect to different decomposition levels. The data is from single channel static parallel imaging reconstruction results for the brain data in Fig. 3. The results showed that the decomposition level of 3 (scales from 0 to 2) is as good as the decomposition level 4 (scales from 0 to 3).